



Cite as
Nano-Micro Lett.
(2022) 14:157

Received: 13 May 2022
Accepted: 3 July 2022
© The Author(s) 2022

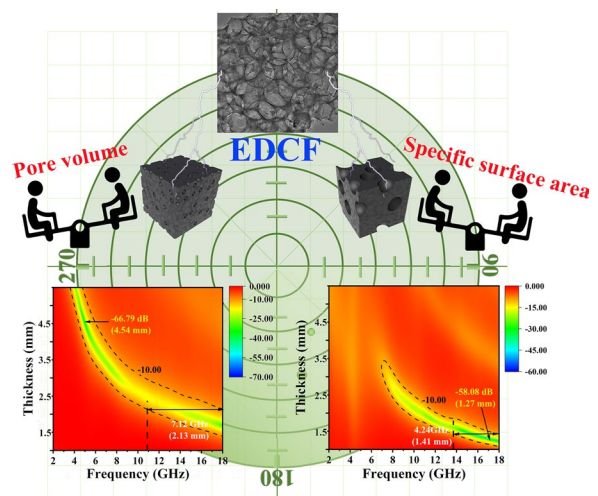
An Equivalent Substitute Strategy for Constructing 3D Ordered Porous Carbon Foams and Their Electromagnetic Attenuation Mechanism

Meng Zhang¹, Hailong Ling¹, Ting Wang², Yingjing Jiang¹, Guanying Song¹, Wen Zhao², Laibin Zhao¹, Tingting Cheng¹, Yuxin Xie¹, Yuying Guo¹, Wenxin Zhao¹, Liying Yuan¹, Alan Meng², Zhenjiang Li¹ ✉

HIGHLIGHTS

- Three-dimensional ordered porous carbon foam with abundant hetero-atoms is successfully prepared through employing silica microspheres template.
- The pore volume and specific surface area are effectively adjusted by an equivalent substitute strategy to investigate their influence on electromagnetic wave absorption performances.
- The attenuation mechanism of electromagnetic wave is clarified according to the contribution of conduction loss and polarization loss on dielectric loss.

ABSTRACT Three-dimensional (3D) ordered porous carbon is generally believed to be a promising electromagnetic wave (EMW) absorbing material. However, most research works targeted performance improvement of 3D ordered porous carbon, and the specific attenuation mechanism is still ambiguous. Therefore, in this work, a novel ultra-light egg-derived porous carbon foam (EDCF) structure has been successfully constructed by a simple carbonization combined with the silica microsphere template-etching process. Based on an equivalent substitute strategy, the influence of pore volume and specific surface area on the electromagnetic parameters and EMW absorption properties of the EDCF products was confirmed respectively by adjusting the addition content and diameter of silica microspheres. As a primary attenuation mode, the dielectric loss originates from the comprehensive effect of conduction loss and polarization loss in S-band and C band, and the value is dominated by polarization loss in X band and Ku band, which is obviously greater than that of conduction loss. Furthermore, in all samples, the largest effective absorption bandwidth of EDCF-3 is 7.12 GHz under the thickness of 2.13 mm with the filling content of approximately 5 wt%, covering the whole Ku band. Meanwhile, the EDCF-7 sample with optimized pore volume and specific surface area achieves minimum reflection loss (RL_{\min}) of -58.08 dB



✉ Zhenjiang Li, zhenjiangli@qust.edu.cn

¹ College of Materials Science and Engineering, College of Electromechanical Engineering, Qingdao University of Science and Technology, Qingdao 266061, People's Republic of China

² State Key Laboratory Base of Eco-Chemical Engineering, College of Chemistry and Molecular Engineering, College of Chemical Engineering in Gaomi Campus, Qingdao University of Science and Technology, Qingdao 266042, People's Republic of China



at 16.86 GHz while the thickness is 1.27 mm. The outstanding research results not only provide a novel insight into enhancement of EMW absorption properties but also clarify the dominant dissipation mechanism for the porous carbon-based absorber from the perspective of objective experiments.

KEYWORDS Porous carbon foam; Electromagnetic wave absorption; Adjustable pore structure; Polarization loss; Attenuation mechanism

1 Introduction

Currently, with the explosive growth of the semiconductor industry and wireless communication technology, electromagnetic radiation and electromagnetic interference are becoming increasingly rampant, which not only affects the normal operation of precision electronic instruments but also poses a serious threat to the health of biological systems [1–3]. In this case, it is extremely urgent to solve the environmental problems of electromagnetic pollution, building an effective protective barrier for people, and ensure the security of private information [4, 5]. Fortunately, electromagnetic wave (EMW) absorbing material can convert electromagnetic energy into other forms, being promoted to a prominence position by countries around the world and becoming a priority development field [6–8].

Experiencing the prosperity of metals and their oxides in the early stage, the industrial community proposes new requirements of "thin, light, wide and strong" for EMW absorbing materials, that is, thin coating thickness, lightweight, wide absorption bandwidth and strong absorption capacity [9–11]. D deservedly, researchers place great expectations on the development of dielectric loss EMW absorbing materials, especially carbonaceous materials with low density, strong corrosion resistance, high thermal stability, good electrical conductivity and adjustable dielectric properties [12–14]. Meanwhile, carbon materials also have the characteristics of diverse microstructure, convenient utilize, simple maintenance, good compatibility with the matrix material etc., which is incomparable to many materials. Over the past decade, a variety of carbonaceous materials, such as carbon nanotubes, carbon fiber, graphene, and carbon quantum dots, have been developed to fight against electromagnetic pollution [15–19].

While retaining the universal advantages of carbon family, three-dimensional (3D) ordered porous carbon nanomaterial with abundant pore structure not only further lowers the density, but also improves the impedance matching of EMW absorbing material, and acquires better multiple

reflection and scattering for incident EMWs, being regarded as one of the ideal candidates for the novel EMW absorbing material [6, 20, 21]. As a result, various strategies (including nanowire/nanosheet self-assembly, sacrifice templates, and biomass derivation/freeze drying) have been designed and implemented to construct the 3D ordered porous carbon-based EMW absorbing materials, and some promising reflection loss (RL) and effective absorption bandwidth (EAB) measurements have been reported, which is also constantly updated [22]. Nitrogen-doped 3D porous reduced graphene oxide aerogels were prepared by Shu and colleagues. By adjusting the doping amount of nitrogen atoms, the microwave absorption performances can be controlled effectively. The measured minimal reflection loss of -56.4 dB and effective absorption broad of 6.8 GHz were achieved at the doping amount of 9.41% [23]. Besides, employing abandoned polyurethane as the sacrificial template of a three-dimensional carbon network, Zhu et al. prepared 3D Fe/Fe₂O₃@porous carbon nanocomposites by simple hydrothermal and thermal treatments, and the optimal sample has a minimum RL of -54.7 dB at a thickness of 1.4 mm and an EAB of 6.4 GHz at 1.9 mm [24]. With wheat straw as raw material, Aslam et al. produced a 3D carbon foam that obtained a minimal reflection loss of -37 dB at 12.1 GHz with the matching thickness of 2.0 mm. At the same time, a wide EAB of 8.8 GHz has also been measured at a matching thickness of 2.5 mm [25]. While Zhao et al. employed peach gum as raw material to prepare honey-comb carbon, which was featured with a 3D porous structure and a reflection loss of -59.4 dB with the effective absorption bandwidth of 4.1 GHz at a matching thickness of 2.0 mm [26]. Nevertheless, there are still some challenges concerning 3D-ordered porous carbonaceous absorbing materials to be addressed. First of all, it is widely accepted that increasing pore volume and specific surface area is the effective approach to optimizing EMW absorption performances of 3D ordered porous carbon materials. Up to date, majority of the reported works adjust the EMW absorption properties only by simply changing the volume of the constructed

pore or addition amount of template microspheres [20, 27]. The variation of pore volume also causes the fluctuation of specific surface area, which seriously interferes in the investigation concerning the influence of the latter on the EMW absorption properties of the 3D ordered porous carbon materials. Due to this, the role of the specific surface area in the EMW absorption properties is still unknown, although it is extremely important for absorbers. Secondly, people obviously invest much effort in pursuing better EMW absorption performances, which is contrast to the less attention paid to the study on the EMW attenuation mechanism of 3D ordered porous carbon materials. Their excellent EMW absorption properties are perfunctorily attributed to the synergistic effect of conduction loss and polarization relaxation caused by the porous structure, which lacks differentiation and accuracy [15, 28]. In other words, the effects of conduction loss and polarization relaxation on the enhancement of EMW absorption performance can not be expounded and enhanced in a targeted way. Therefore, the optimization of EMW absorption performance of 3D ordered porous carbon-absorbing materials can only rely on the semi-empirical attenuation mechanism [29, 30].

In order to solve the above two significant problems and sweep away the obstacle to the development of 3D ordered porous carbon-absorbing materials, the products with the controlled pore volume and specific surface area should be first prepared. It is well known that biomass-derived porous carbon with the characters, such as environment friendliness, wide sources of raw materials, feasible technique methods, high yields, low production cost and intrinsic porous structure plays an important role in EMW absorbing areas. Eggs are rich in protein, cholesterol and lecithin matter, and there are also abundant N, O, S, P, etc. hetero-atoms embedded in the derived carbon lattice, endowing the product in situ doping effect and some peculiar properties. More importantly, the egg liquid possesses good fluidity and plasticity, and the morphology and microstructure can be easily adjusted through the curing and subsequent carbonization process. In this case, the size and ratio of created pores can regulate in an effective manner, which is also beneficial for the enhancement of the interface polarization and dielectric loss, as well as EMW absorption properties. Herein, using the egg as biomass raw material and silica microspheres with the diameter of 200 nm as removable templates, a novel egg-derived porous carbon foam (EDCF) with uniform pore

diameter and different pore volume was firstly prepared by adjusting the addition amount of silica. Thus, the widest effective absorption bandwidth (EAB) value of 7.12 GHz was achieved at the thickness of 2.13 mm. Following the equivalent replacement strategy, a group of EDCF samples with the same porosity (pore volume) but different specific surface area and the same specific surface area but different pore volume were also respectively constructed to investigate the influence of individual pore volume and specific surface area on the EMW absorption performances. While revealing the influence of porosity and specific surface area on electromagnetic wave attenuation, the EDCF sample with optimal porosity and specific surface area was obtained. Moreover, its minimum RL is -58.08 dB at the thickness of 1.27 mm. This work not only fills in the blank of the influence of pore volume and specific surface area on the EMW absorption performance of porous carbon nanomaterials but also provides a promising strategy for the development of ultra-light porous carbon EMW absorbing material.

2 Experimental Section

Employing the egg as biomass raw material and the self-made silica microsphere as the template, 3D-ordered porous EDCF was prepared through freeze drying, subsequent calcination, and hydrofluoric acid etching processes. The specific steps are as follows (shown in Fig. 1a): Firstly, the uniform silica microsphere (about 200 nm in diameter) prepared by the Stöber method was introduced into a certain mass of egg liquid (about 50 g) and mechanically stirred for two hours to fully mix them [19, 31, 32]. Then, the egg liquid mixture was steamed at 100 °C for 20 min, and the cooked sample was treated for 48 h by vacuum freezing and drying technology. Subsequently, the lyophilized precursor was calcined at 850 °C for 2 h under the protection of argon atmosphere, followed by the 3D-ordered porous egg-derived carbon with embedded uniform silica microspheres (EDC@SiO₂ nanocomposites) being collected. After soaking in hydrofluoric acid for 48 h, the silica template was removed completely, and the residual product was rinsed with deionized water several times until the solution reached neutral. Finally, the sample was dried completely, and the 3D ordered porous EDCF was obtained. In addition, a series of EDCF samples with different porosity (pore volume) were prepared by

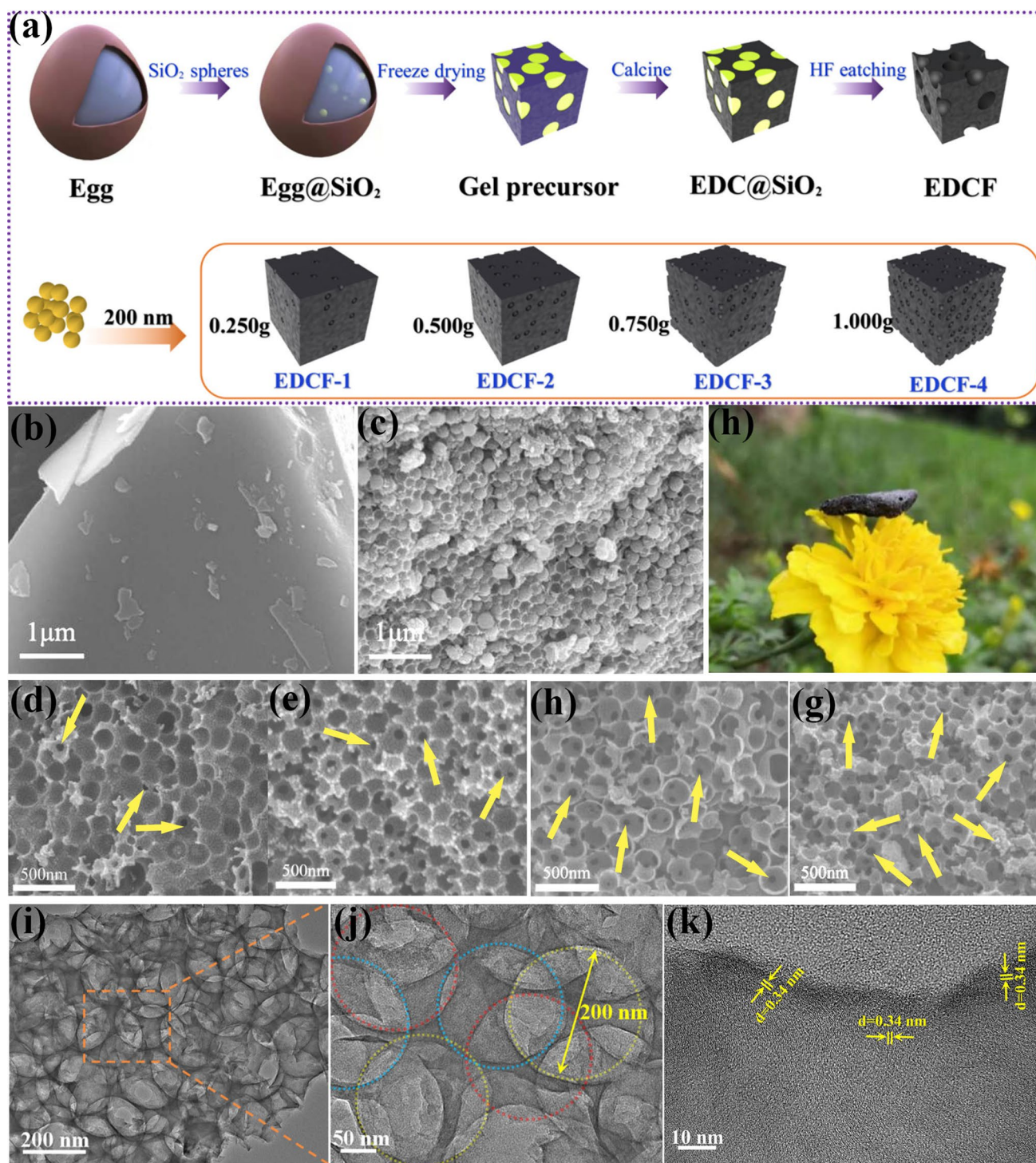


Fig. 1 **a** Schematic illustration of the synthesis process of EDCF samples with different amounts of 200 nm silica microsphere addition; **b** SEM images of EDC and **c** EDC@SiO₂ nanocomposites; **d–g** SEM images of EDCF-1 ~ EDCF-4 samples; **h** the photograph of free-standing EDCF; **i, j** representative TEM images and **k** HRTEM images of EDCF samples

adjusting the addition amount of SiO₂ microspheres to 0.25, 0.5, 0.75, and 1.0 g, which was named EDCF-1, EDCF-2, EDCF-3, and EDCF-4, respectively.

3 Results and Discussion

3.1 Design and EMW Absorption Properties of Ordered Porous EDCF

Figure 1b displays a typical SEM image of EDC. Obviously, the surface of the as-synthesized sample is smooth without pores or fluctuation in the absence of silica participation. Figures 1c and S1 show the SEM images of egg-derived carbon embedded with silica template microspheres (EDC@SiO₂ nanocomposites), and a large number of silica microspheres with the diameter of about 200 nm have been evenly dispersed in the sample. To explore the effect of silica microsphere addition amount on the morphology evolution of EDCF samples, the SEM images of various samples were shown in Fig. 1d–g. Compared with the origin EDC and EDC@SiO₂ samples, the silica microspheres were completely removed, leaving a large number of uniform spherical pores with the diameter of about 200 nm, which is consistent with the size of silica. Clearly, as the amount of silica microsphere addition increases, the created pore amount in EDCF samples also gradually increases, and the skeleton proportion (the enclosed region constructed by adjacent spherical pores, as shown in Fig. S2) gradually decreases. Since the employed silica has the same diameter, it can be inferred that the created specific surface area and pore volume of EDCF-2, EDCF-3, and EDCF-4 are 2, 3, and 4 times higher than that of EDCF-1, respectively (Tables S1 and S2). Besides, the density of the obtained EDCF samples also gradually decreases, as exhibited in Fig. 2a. Due to the delicate wall structure and high porosity, the density value of EDCF-1, EDCF-2, EDCF-3, and EDCF-4 is as low as 0.093, 0.064, 0.043, and 0.038 g cm⁻³, accordingly, thus being able to rest on the petals easily, showing an attractive advantage of ultra-lightweight character, as shown in Fig. 1h. Interestingly, some mesopores with the diameter of about 40 nm appear at the bottom of the created pore (as shown by yellow arrow) that increases gradually from EDCF-1 to EDCF-4 in quantity, which can result from the increasing packing density of silica microspheres as the increased addition amount of silica microspheres. Due to mesoporous structure, EDCF

samples can constitute a penetrative network structure, which is not only favorable for removing the deeply embedded silica microspheres but also provides some additional channels for the EMW to enter the internal samples besides the created pores [33, 34].

To further explore the microstructure of EDCF samples, TEM characterization was implemented, and the typical results were revealed in Fig. 1i–k. Based on Fig. 1i, the dense accumulated pores mould the sample to form an ordered network structure. According to the aggregation-induced charge transport theory, the EDCF with the porous conductive network not only provides the capacity for multiple reflection and scattering but also enhances the conduction loss [35]. Obviously, the pores located in different layers stack together and lead to different lightness and shade contrast in the vertical direction, while the bright area corresponds to the created pore with good light transmittance, and the dark area is assigned to the carbon skeleton region with poor light transmittance. Figure 1j shows a partial enlargement image of the pores in different layers, captured from the marked area in Fig. 1i, and can be depicted by dotted circles in different colors. Figure 1k displays a typical HRTEM image of the constructed carbon skeleton, in which the lattice fringes were not recorded, indicating that the as-obtained carbon was in amorphous state [36]. However, it is necessary to note that some nano-crystalline graphite in the form of vortex/onion-like structure can be detected (as shown in the circle), which is of great importance for improving the conductivity and conduction loss of carbonaceous absorbing materials [37].

To determine the phase composition of the obtained EDCF samples, the XRD analysis was conducted, and the corresponding patterns were presented in Fig. 2b. Two broad diffraction peaks located at 26° and 43° could be assigned to the characteristic peaks of (002) and (100) crystal planes of carbon, which originates from amorphous carbon and graphite respectively. In addition to that, the broad contour and low intensity manifest that the existing main phase of EDCF samples is amorphous carbon, which is consistent with the TEM results of Fig. 1k [38]. Moreover, Raman spectra of various EDCF samples were recorded to further investigate the microstructure information of carbon components, as displayed in Fig. 2c. Then, it can be found that all of the four samples display broad D-band and G-band located around 1300 and 1580 cm⁻¹, which is caused by defects and disorder structure of the materials and in-plane stretching

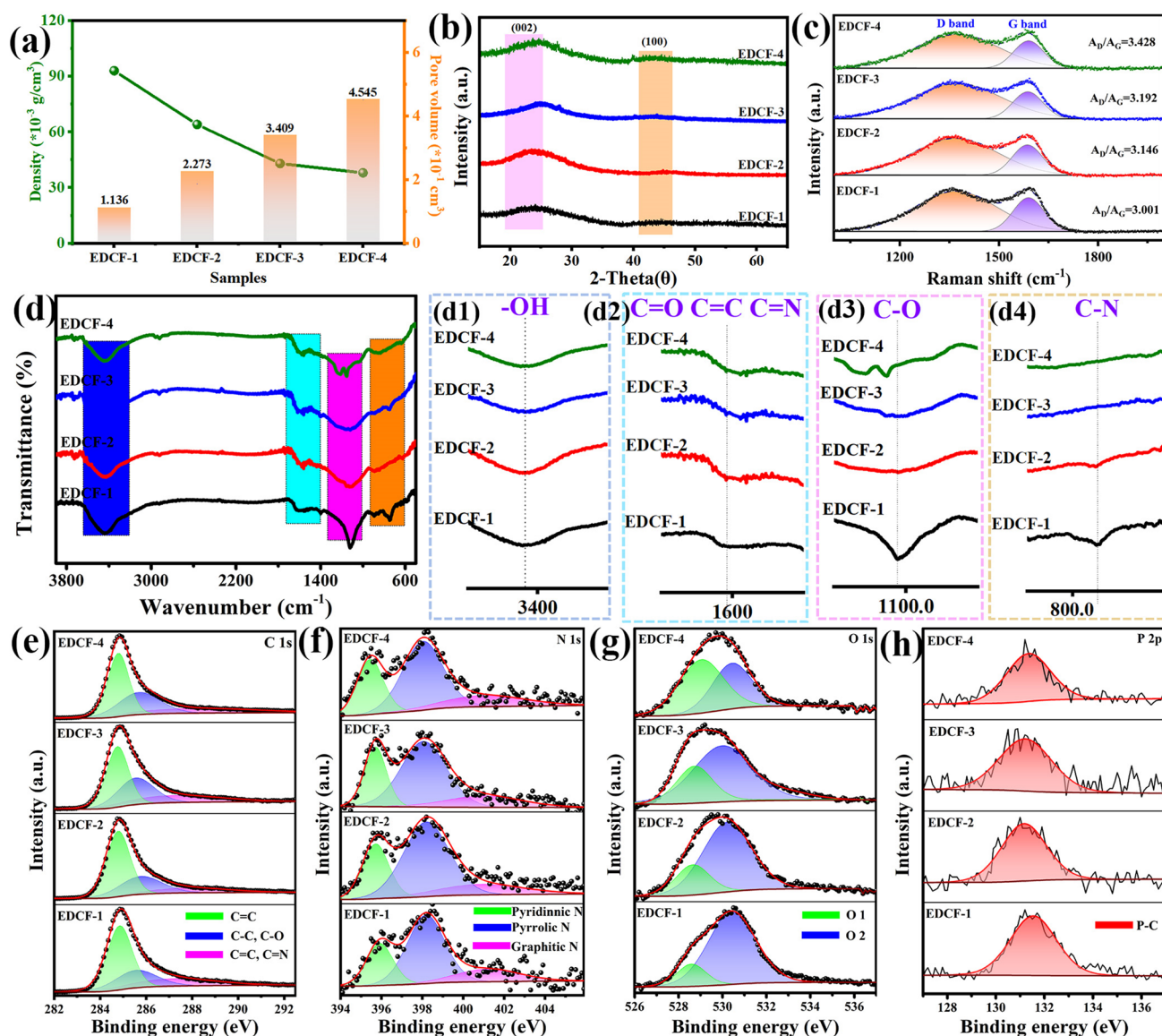


Fig. 2 a Variation of density, pore volume and specific surface area of EDCF samples with different addition amount of 200 nm silica microspheres; b XRD patterns, c Raman spectra, d FT-IR spectra and partial enlarged images of FT-IR captured from marked area in Fig. 2d (d1 ~ d4); high-resolution XPS spectra of e C 1s, f N 1s, g O 1s and h P 2p of EDCF-1 ~ EDCF-4 samples

vibration of carbon atom sp^2 hybrid respectively [39]. It is well known that high-temperature heat treatment plays a crucial role in the graphitization degree, and the EDCF samples prepared at the same temperature achieve similar graphitization degree. According to the integral area values of D band and G band, the graphitization degree can be evaluated by the A_D/A_G values and it is 3.001, 3.146, 3.192, and 3.428 respectively, indicating their main amorphous state [40, 41]. The slight increase tendency may be aroused by the numerous intrinsic N, O, etc. hetero-atom induced defects within

carbon structure in the form of asymmetric oxygen-containing groups, which is conducive to the interfacial polarization and dipole polarization [42]. It is worth mentioning that the presence of amorphous carbon prevents the electron movement, and results in a poor conduction loss.

Figure 2d is the FT-IR spectra recorded from various EDCF samples with different addition amount of 200 nm silica microspheres, and Fig. 2d1–d4 correspond to the partial enlarged images of each characteristic peak appearing in various wavenumber segments, respectively. It can be seen

that the curve tendency of FT-IR spectra is similar to each other without significant change, and the location of corresponding characteristic peaks is basically unchanged, revealing that the types of functional groups adhered to the surface of EDCF samples are not affected by the increased pore. Besides, the absorption peak at approximately 3400 cm^{-1} corresponds to the adsorbed hydroxyl ($-\text{OH}$) that may come from adsorbed water of the sample [43]. Multiple peaks at around 1600 cm^{-1} can be assigned to the characteristic peak of $\text{C}=\text{O}$, $\text{C}=\text{C}$, and $\text{C}=\text{N}$, while the peak at about 1100 cm^{-1} may be caused by $\text{C}-\text{O}$ bond, and that near 800 cm^{-1} is mainly attributed to the stretching vibration of $\text{C}-\text{N}$ bond [44–47]. These polar functional groups are considered as the dipole polarization center, which can induce the turning-direction polarization, thus enhancing the polarization loss and EMW absorption capacity of EDCF [48]. From the curve fitting results shown in Fig. 2d1, it can be observed that the integral area of the $-\text{OH}$ absorption peak gradually increases from EDCF-1 to EDCF-4. Generally, these $-\text{OH}$ groups are mainly adsorbed on the spherical surface of pores. The larger the specific surface area is, the more $-\text{OH}$ groups are adhered to the surface. Different from the $-\text{OH}$ group existing on the surface, $\text{C}=\text{O}$, $\text{C}=\text{C}$, $\text{C}=\text{N}$, and $\text{C}-\text{O}$, $\text{C}-\text{N}$ bonds are mainly originated from the combination of N, O hetero-atoms in the carbon structure, which is the main cause of defect dipole polarization. Furthermore, the N and O atoms are evenly distributed in the mixed egg liquid, and their content is in inverse proportion to the total pore volume. With the increase of the created pore, the amount of $\text{C}=\text{O}$, $\text{C}=\text{C}$, $\text{C}=\text{N}$ and $\text{C}-\text{O}$, $\text{C}-\text{N}$ gradually decreases, which may weaken the dipole polarization of EDCF.

The chemical bonds and electron state of the four EDCF samples were characterized by XPS, and the corresponding results were shown in Fig. 2e–h. Figure 2e displays the C 1s spectra, which can be decomposed into three independent peaks at 284.6, 285.3, and 286.3 eV, corresponding to $\text{C}-\text{C}/\text{C}=\text{C}$, $\text{C}=\text{N}$, and $\text{C}=\text{O}$, respectively [49]. $\text{C}=\text{N}$ and $\text{C}=\text{O}$ bonds are beneficial to the improvement of the conductivity of the material, leading to excellent conduction loss and enhancing the EMW absorption performance of EDCF samples. Interestingly, the corresponding integral area of $\text{C}-\text{C}/\text{C}=\text{C}$ bonds remains unchanged, while that of the $\text{C}=\text{N}$ and $\text{C}=\text{O}$ bonds in the EDCF samples decreases with the enhancement of the pore number. As exhibited in Fig. 2f, N 1s spectra of EDCF samples can be divided into three integral peaks, located at 398.3, 400.6, and 403.7 eV

separately, which represent pyridine type N, pyridine type N and oxidized N [50]. It is worth noting that the relative intensity of the pyridine nitrogen peak (or the intensity ratio of pyridine nitrogen to pyrrole nitrogen) gradually decreases as the created pore increases, which is in line with the change of $\text{C}=\text{N}$ and $\text{C}-\text{N}$ bonds of FT-IR spectra in Fig. 2d2. Figure 2g that displays the O 1s peak, which can be divided into two stripping peaks appearing at 528.6 and 530.7 eV, corresponding to defect oxygen and surface adsorbed oxygen, respectively [51]. Besides, the amount of the defect oxygen decreases with the increase of pore numbers, while the amount of surface adsorbed oxygen in EDCF samples increases gradually. EDCF-4 achieves the largest specific surface area and pore volume, suggesting its least carbon skeleton volume. Therefore, the maximum of adsorbed $-\text{OH}$ groups and the minimum of N, O-containing bonds can be simultaneously accomplished. Moreover, Fig. 2h displays the P 2p spectra of phosphorus elements corresponding to the P–C bond, whose relative intensity slightly weakens with the increased pore. In particular, various N and O atom doping in the carbon conductive networks brings a large number of internal defects and promotes the movement of electrons, generating some dipole polarization loss under an applied electromagnetic field.

To evaluate the EMW absorption performances of the EDCF samples, it is necessary to investigate the variation of electromagnetic parameters. Carbon is usually considered as a dielectric loss absorbing material because of its negligible magnetic loss and complex permeability. As can be seen from the curves of the real part (μ') and imaginary part (μ'') of permeability in Fig. S3a, b, all samples are featured with the similar permeability value, and synchronous variation is kept with the change of frequency. It is speculated that the slight fluctuation phenomenon may be concerned with the magnetic moment originated from disordered carbon structure (internal hetero-atom induced defects). However, the values of μ' and μ'' stabilize near 1 and 0 respectively, indicating that the magnetic loss can be reasonably neglected [52]. In this work, the real part (ϵ') and imaginary parts (ϵ'') of the permittivity of EDCF samples are what we care about, which represent the electric field energy storage and attenuation ability of an absorber. In addition, the complex permittivity (ϵ_r) of all samples in the frequency range of 2–18 GHz was captured at room temperature, which can be represented by the following equations [53, 54]:

$$\varepsilon_r = \varepsilon_\infty + \frac{\varepsilon_s - \varepsilon_\infty}{1 + j2\pi f\tau} = \varepsilon' - j\varepsilon'' \quad (1)$$

$$\varepsilon' = \varepsilon_\infty + \frac{\varepsilon_s - \varepsilon_\infty}{1 + (2\pi f)^2\tau^2} \quad (2)$$

$$\varepsilon'' = \frac{2\pi f\tau(\varepsilon_s - \varepsilon_\infty)}{1 + (2\pi f)^2\tau^2} \quad (3)$$

where ε_∞ is the optical dielectric constant; ε_s refers to the static dielectric constant; τ denotes the relaxation time, and f indicates the frequency. Figure 3a, b shows the variation curves of ε' and ε'' versus frequency in the frequency range of 2–18 GHz. Obviously, the complex permittivity of EDCF samples can be regulated by adjusting the addition amount of silica. The ε' values of EDCF samples gradually decrease with the increase of the frequency, which can be attributed to the hysteresis of dielectric polarization caused by the variation of electromagnetic field (chromatic dispersion) [55]. Noteworthy, the smallest ε' value appears in the EDCF-1 with the minimum number of pores, and the ε' curves of EDCF-2 display the largest values. In the low-frequency range, the ε' value of EDCF-3 is larger than that of EDCF-4, but both values change synchronously with the increase of frequency in the middle and high-frequency range. As exhibited in Fig. 3b, EDCF-1 has the smallest ε'' value, and EDCF-3 achieves the largest ε'' value, indicating its strongest EMW attenuation capacity. Other than that, EDCF-2 and EDCF-4 have roughly the same ε'' values. Furthermore, Fig. 3c shows the dielectric loss ($\tan\delta_e = \varepsilon''/\varepsilon'$) curves. It can be found that the variation of $\tan\delta_e$ is more dependent on the imaginary part of permittivity, and in the meanwhile, EDCF-3 acquires the largest value in the measured frequency, which changes more sharply than that of the other three samples, revealing its excellent high-frequency response. As shown in Fig. S3c, the magnetic loss tangent ($\tan\delta_\mu = \mu''/\mu'$) values are always equal to 0, suggesting that no magnetic loss was exerted on the EMW attenuation for EDCF samples. Moreover, the Cole–Cole curve can effectively demonstrate the polarization relaxation phenomenon of the absorber, and each semicircle in the curve corresponds to a Debye relaxation process. The value can be calculated by the following equations [56, 57]:

$$\left(\varepsilon' - \frac{\varepsilon_s + \varepsilon_\infty}{2}\right)^2 + (\varepsilon'')^2 = \left(\frac{\varepsilon_s - \varepsilon_\infty}{2}\right)^2 \quad (4)$$

Figures 3d and S4 exhibit the Cole–Cole curves of EDCF samples. It can be determined that all of the EDCF samples display several semicircles marked in red colour, suggesting

that multiple Debye relaxation phenomena occur, which can effectively dissipate the energy of the incident EMW [58]. In addition, EDCF-2 produces the most Debye dipole relaxation process, resulting in the largest ε' value, which is consistent with Fig. 3a. Generally, the dielectric loss and ε' curve variation of the absorber are mainly influenced by dipole polarization relaxation and interfacial polarization. With the increase of pores, the surface of EDCF produces more dangling bonds/absorbed functional groups and few N, O, and P hetero-atoms, leading to strong interfacial polarization and weak defect-induced dipole polarization. To some extent, the ε' value can be considered as the result of the competition between the interfacial polarization and the internal dipole polarization of the products. Noteworthy, previous works have pointed out that the slope of the linear end of Cole–Cole curves represents the conduction loss of the absorbing materials. Interestingly, the slope of Cole–Cole captured from EDCF samples gradually decreases with the increase of the pore number, implying their decreased conduction loss [59].

It is well known that the dielectric loss of the absorbing materials can be classified into conductance loss and polarization loss. For conduction loss, the value is closely associated with dielectric conductivity. As the graphitization degree is typically dominated by high treatment temperature, the EDCF samples prepared at the same temperature obtain similar graphitization degree and electron migration capability, meaning that the conduction loss of the EDCF sample is weak [60, 61]. For polarization loss, the main contribution can be ascribed to interface polarization and dipole polarization, because the electron/ion displacement polarization phenomenon doesn't seem to have an impact on ε_r . In order to clarify the source of dielectric loss of the EDCF samples, the conduction loss and polarization loss should be analyzed in detail, which can be measured according to the following equation [62, 63]:

$$\varepsilon'' = \varepsilon_p'' + \varepsilon_c'' = (\varepsilon_s - \varepsilon_\infty) \frac{2\pi f\tau}{1 + (2\pi f)^2\tau^2} + \frac{\sigma}{2\pi f\varepsilon_0} \quad (5)$$

where ε_p'' represents the contribution of polarization loss; ε_c'' is the contribution of conduction loss; σ refers to the dielectric conductivity, and ε_0 ($\varepsilon_0 = 8.854 \times 10^{-12}$ F m⁻¹) denotes the vacuum permittivity. The theoretical fitting calculation values of σ for various EDCF samples were shown in Fig. 3e, which exhibits opposite varying tendency with the pore volume, consistent with the EIS spectrum (Fig. 3f) [64]. In fact, the porous EDCF samples can be served as a complex made up of solid medium and spherical pores. Moreover, in

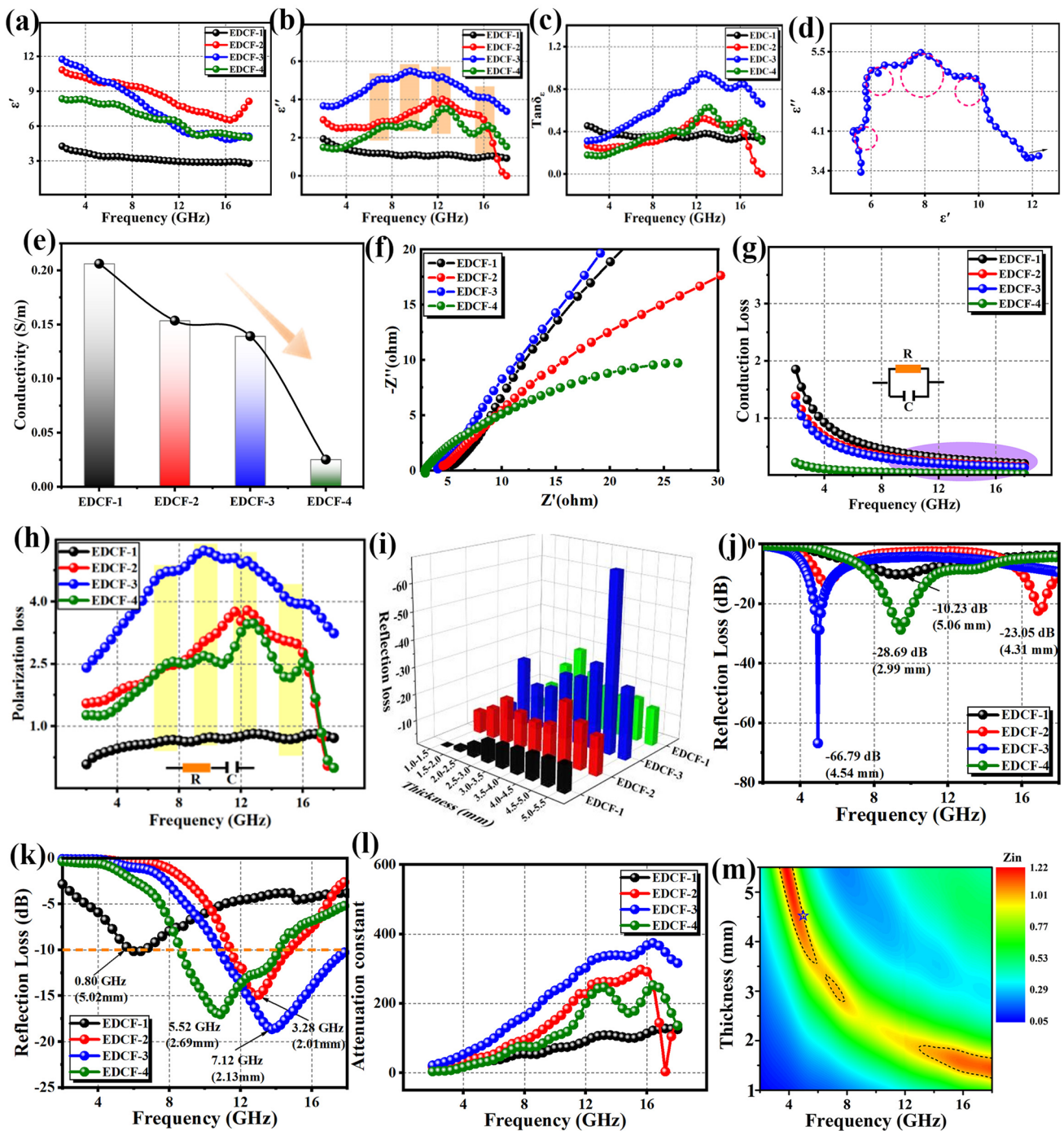


Fig. 3 **a** The real part and **b** the imaginary part of the complex permittivity for various EDCF samples; **c** tangent of dielectric loss of the EDCF samples; **d** Cole–Cole curve of EDCF-3; **e** conductivity; **f** EIS spectrum of EDCF samples; **g** conduction loss values and **h** polarization loss values of various EDCF samples versus frequency; **i** comparison of the RL values of various EDCF samples at different thickness; **j** comparison of the minimum RL curves and **k** the widest EAB curves of different EDCF samples at their respective optimum thickness; **l** attenuation constant of EDCF samples; **m** impedance matching of EDCF-3

this work, a larger number of holes mean higher resistivity (poor conductivity). Subsequently, the conduction loss and polarization loss curves were shown in Fig. 3g, h. In addition, the equivalent circuit can be regarded as the parallel and series circuit of resistance and capacitor, respectively [65, 66]. In Fig. 3g, the conduction loss curves display the same decrease trend with the increasing frequency, and the corresponding values reach 0.2~0.3 in the high-frequency range. The polarization loss was also calculated and exhibited in Fig. 3h, and the variation tendency and the frequency of polarization loss peaks of the corresponding results were very close to the resonance of ϵ'' curves, which is also in well accord with the Debye relaxation phenomenon. Furthermore, it can be found that polarization loss is slightly larger than conduction loss in the frequency range of about 2~8 GHz, but reaches one order of magnitude higher than the value of conduction loss in the frequency range of about 8~18 GHz. The dielectric loss originated from the synergistic effect of conduction loss and polarization loss in S-band and C band. However, the contribution of conduction loss with very small value can be neglected in X band and Ku band, which is mainly provided by polarization loss. As demonstrated in Fig. 3i, their relationship can be briefly described as the unity of opposites.

According to transmission line theory, the reflection loss (RL) value can be calculated by the following equations [19, 67, 68]:

$$Z_{in} = Z_0 \sqrt{\frac{\mu_r}{\epsilon_r} \tanh \left[j \left(\frac{2\pi f d}{c} \right) \sqrt{\mu_r \epsilon_r} \right]} \quad (6)$$

$$RL \text{ (dB)} = 20 \log \left| \frac{Z_{in} - Z_0}{Z_{in} + Z_0} \right| \quad (7)$$

where Z_0 refers to the impedance of free space; Z_{in} represents the input impedance; ϵ_r ($\epsilon_r = \epsilon' - j\epsilon''$) means the complex permittivity; μ_r ($\mu_r = \mu' - j\mu''$) denotes the complex permeability; f signifies the frequency of the input EMW; d is the thickness, and c represents the light velocity. Fig. S5 shows the RL curves of various EDCF samples in the frequency range of 2~18 GHz at different matching thicknesses. Obviously, the located frequency of the minimum reflection loss value (RL_{min}) for EDCF samples displays a shift towards lower frequency with the increase of corresponding thickness. In addition, EDCF-1 presents poor EMW absorption performance with the RL_{min} of -10.23 dB at 5.06 mm thickness, and its effective absorption bandwidth (EAB, < -10 dB) is exceedingly narrow. For EDCF-2, EDCF-3, and EDCF-4 samples, the RL and EAB can be effectively changed by adjusting the thickness in the frequency range of 4~18 GHz. Compared with other samples,

the EDCF-3 gains excellent EMW absorption performances with the RL_{min} of -66.79 dB at the thickness of 4.54 mm. Meanwhile, it achieves the widest EAB of 7.12 GHz at 2.13 mm thickness. When the matching thickness is greater than 4 mm, EDCF-1 and EDCF-4 capture two RL_{min} peaks in C band and Ku band, respectively. In addition, with the increases of the pore number, the located frequency of the RL_{min} shifts towards low frequency, while the EAB value is mainly concentrated in the X-band and Ku band. The attenuation constant (α) of the samples was measured, which is strongly associated with the dissipation ability of electromagnetic waves [69].

$$\alpha = \frac{\sqrt{2}\pi f}{c} \sqrt{(\mu''\epsilon'' - \mu'\epsilon') + \sqrt{(\mu''\epsilon'' - \mu'\epsilon')^2 + (\mu'\epsilon'' + \mu''\epsilon')^2}} \quad (8)$$

Figure 3m shows the α values of various EDCF samples. Obviously, the curves display a similar sequence of samples as Fig. 3c (EDCF-3 > EDCF-2 > EDCF-4 > EDCF-1) in the frequency range of 2~18 GHz, suggesting the dominant effect of dielectric loss on the α values. Impedance matching is an important indicator for evaluating the EMW entering the material, which can be evaluated by Z_{in} value according to Eq. 6. Ideally, when the input impedance matching of the absorbing material is equal to the free space impedance, it is implied that the EMW was introduced completely. Figures 3n and S6 show the Z_{in} contour chart of EDCF samples at different frequencies and thicknesses. It can be seen that the value of EDCF-3 fluctuates slightly around $Z_{in} = 1$, indicating its good impedance matching, and the EMW can enter the sample effectively, which is also a prerequisite for achieving excellent EMW absorption performances. Moreover, Fig. S7 presents the normalized impedance matching characteristic of EDCF samples. Then, it can be found that better RL_{min} and EAB values appear in the EDCF-3 with Z_{in} value approaching 1 although the α value at the frequency of RL_{min} is far less than that of other samples, revealing that the decisive effect of impedance matching on EMW absorption performances.

To clarify the influence of pore volume on the electromagnetic parameters and EMW absorption performances, it is necessary to ensure a single variable, that is, avoiding the interference of and specific surface area. Therefore, two EDCF samples (EDCF-5 and EDCF-6) were constructed under the assist of silica microspheres with the diameter of 500 nm and 1 μm respectively (as shown in Fig. 4a), and the addition content was fixed at 0.75 g, which

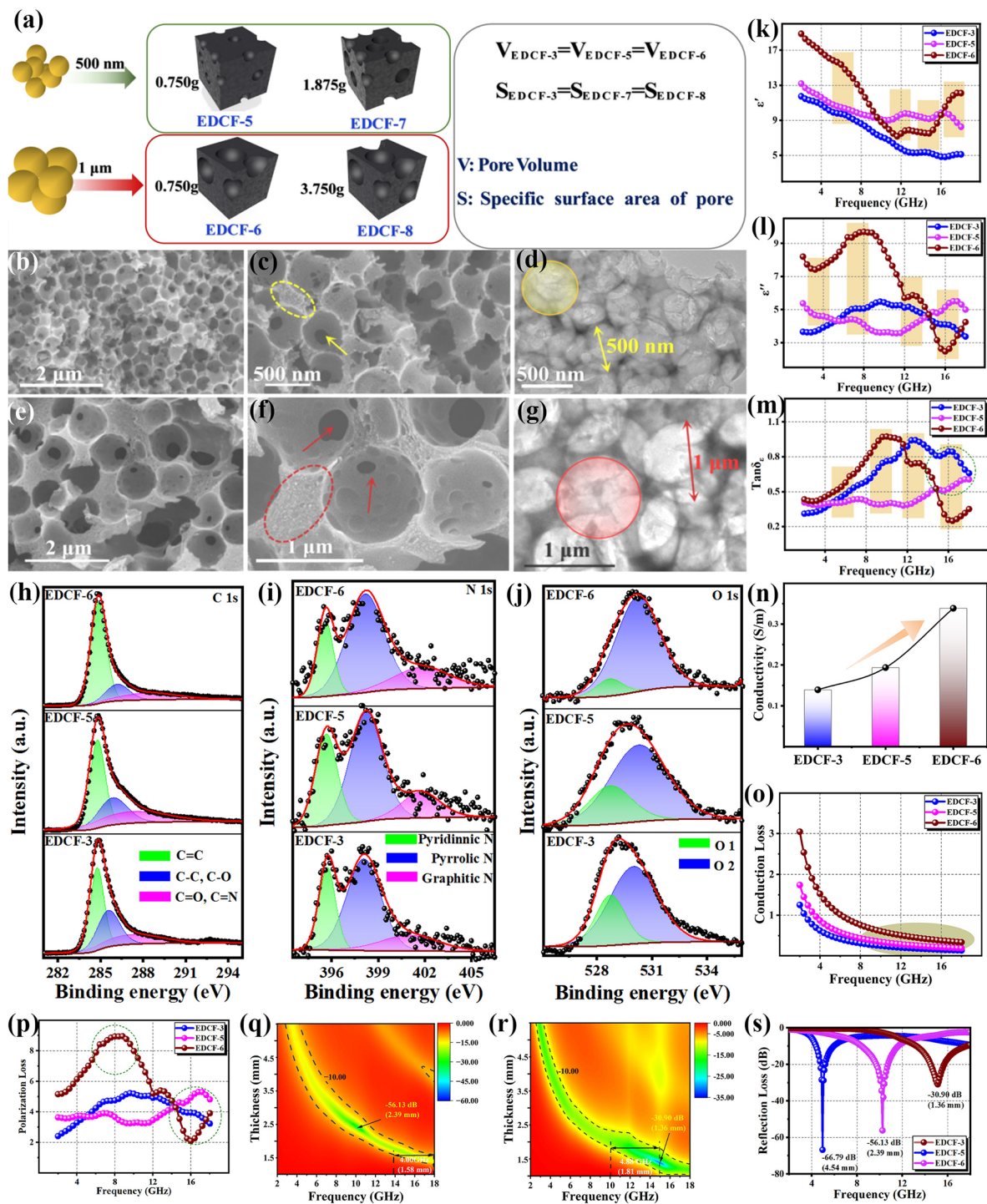


Fig. 4 a Schematic diagram of EDCF-5 and EDCF-7 constructed using 500 nm silica microspheres, and EDCF-6 and EDCF-8 constructed using 1 μm silica microspheres; b, c SEM images and d TEM image of EDCF-5 sample; e, f SEM images and g TEM image of EDCF-6 sample; high-resolution XPS spectra of h C 1s, i N 1s, and j O 1s of EDCF-3, EDCF-5 and EDCF-6 samples; k the real part and l the imaginary part of the complex permittivity and m dielectric loss tangent for EDCF samples with the same pore volume; n conductivity values; o conduction loss curves and p polarization loss curves of EDCF-3, EDCF-5 and EDCF-6 samples; q RL diagram versus frequency of EDCF-5 and r EDCF-6 at different thickness; s comparison of the RL values of various EDCF samples at their optimal thickness

is consistent with EDCF-3. Obviously, EDCF-3, EDCF-5, and EDCF-6 are featured with the same pore volume ($V_{\text{EDCF-3}} = V_{\text{EDCF-5}} = V_{\text{EDCF-6}}$) but different specific surface areas ($S_{\text{EDCF-3}} > S_{\text{EDCF-5}} > S_{\text{EDCF-6}}$). A large number of uniform pores with the diameter of 500 nm equivalent to the employed silica microsphere template have been inserted into the carbon skeleton of EDCF (as shown in Fig. S8). Figure 4b, c are the SEM images of EDCF-5, and it can be observed that some mesoporous structures similar to EDCF-3 were formed at the bottom of the pore. Figure 4d shows a typical TEM image of EDCF-5. Obviously, a large number of pores with the diameter of 500 nm in different layers accumulate successively and fill into the as-prepared product. Besides, no obvious lattice structure is detected at the discernible edge position, indicating that the obtained carbon material exists in amorphous state. Figures 4e, f exhibit the SEM images of EDCF-6, and the diameter of the created pore is increased to 1 μm while a larger silica microsphere template is used. On the one hand, as the diameter of the employed silica microsphere increases, the number of pores significantly decreases (as depicted in the field of vision), whereas, on the other hand, the volume of an individual enclosed carbon skeleton area (as shown by the red arrow) is accordingly increased. Moreover, in Fig. 4g, a typical TEM image of EDCF-6 appears, revealing a uniform pore diameter of about 1 μm , and there is still abundant space for accommodating more silica microspheres.

Figure S9 displays the XRD pattern and Raman spectra captured from the EDCF samples with the same pore volume (EDCF-3, EDCF-5, and EDCF-6), respectively. Clearly, all of the three EDCF samples display the same phase and microstructure, indicating that the composition was not affected by the size of created pores. As shown in Fig. S10, due to the same volume proportion of carbon skeletons, the relative intensity of carbon-containing bonds located at 800, 1100, and 1600 cm^{-1} keeps unchanged, while the characteristic peak at around 3400 cm^{-1} assigned to the adsorbed -OH group is featured with a reduced relative intensity from EDCF-3 to EDCF-5 and EDCF-6 with the decrease of specific surface area. Figure 4h, j displays the high-resolution XPS spectra of C 1s, N 1s, and O 1s recorded from EDCF-3, EDCF-5, and EDCF-6, accordingly. In C 1s spectra (Fig. 4h), the bonding energy, relative intensity and the integral area of each divided peak from the three EDCF samples are roughly identical. In general, nitrogen atoms are mainly distributed in the carbon skeleton, and its

relative content is in inverse proportion to the pore volume. Obviously, the integral area ratios of pyridinic N to pyrrole N, and pyridinic N to graphite N of above three EDCF samples are roughly identical, demonstrating their same amount. In Fig. 4j, the relative intensity and integral area of peak O1 decrease while those of peak O2 keep constant, implying that the smaller the created pore diameter (higher specific surface area), the more functional group adsorbed on the surface when the EDCF samples have the same pore volume. Furthermore, the interfacial polarization generated by the adsorbed functional group will be less for EDCF-6 compared with EDCF-3 and EDCF-5.

Figure 4k, l present the variation curves of the ϵ' and ϵ'' values captured from the three samples as a function of frequency. Clearly, the ϵ' values of EDCF-5 and EDCF-6 are larger than that of EDCF-3 in most measured frequencies, and EDCF-5 displays a similar variation tendency to that of EDCF-3 with the increase of frequency. The ϵ' curve of EDCF-3 and EDCF-5 decreases gradually, while that of EDCF-6 decreases first and then increases when the maximum value is obtained in the frequency range of 2 ~ 10 and 16 ~ 18 GHz, indicating its good storage capacity of electric field energy. The maximum ϵ' value was occupied by EDCF-5 in the frequency range of 10 ~ 16 GHz. As can be seen from Fig. 4l, the ϵ'' values of EDCF-5 slightly fluctuate between 3 and 5 by adjusting the measured frequency. For EDCF-6, the ϵ'' values reach the maximum of 9.70 at 8 GHz, and then rapidly decrease to the minimum value at 16 GHz followed by a slight increase. In the medium and high-frequency range, EDCF-6 has larger values than EDCF-3 and EDCF-5, revealing its excellent dielectric loss capacity. However, lower values are collected in the high-frequency range. It is well known that these maximum or minimum values generally can be regarded as resonance peaks, which is corresponding to different polarization or relaxation processes. Interestingly, EDCF-3 possesses the same carbon skeleton and larger specific surface area as EDCF-5 and EDCF-6, suggesting that EDCF-3 may produce more interfacial polarization. Nevertheless, EDCF-6 is given the larger value of complex permittivity when compared with EDCF-3. It can be speculated that the value may be related to the diameter of pores. Figure 4m shows the curve of $\tan\delta_e$ values with frequency variation, and the overall tendency of each sample is similar to the curves in Fig. 4l, revealing the stronger dielectric loss capacity of EDCF-3 and EDCF-6 for the incident EMW. In the medium and low-frequency ranges

of 2~12 GHz, the largest $\tan\delta_e$ value of EDCF-6 appears. However, EDCF-3 achieves the largest $\tan\delta_e$ values in the high-frequency range of 12~18 GHz.

Figure S11 shows the Cole–Cole curves of EDCF samples with the same pore volume. It can be discovered that all of the three samples have multiple relaxation processes, and the appearing frequency of Debye relaxation marked by dotted circles almost corresponds to the frequency of resonance peaks of ϵ'' and ϵ' . The dielectric conductivity was calculated and exhibited in Fig. 4n, and the values increase gradually with the increase of silica size and specific surface area. Accordingly, as shown in Fig. 4o, the EDCF-6 sample with 1000 nm pore diameter achieves higher conductive loss, which is generally consistent with the tail slope of Cole–Cole curves and may provide some reference for analyzing the conductive loss of absorbing materials. It can be speculated that when the EDCF samples were endowed with the same pore volume, the smaller the specific surface area is, the fewer surface adsorption functional groups it contains, and the electron quenching phenomenon or the number of bound electrons will also be reduced, which effectively enhances the conductivity and increases the conduction loss of the sample. At the same time, as shown in Fig. 4p, the polarization loss of EDCF-6 increases gradually in the range of 4~8 GHz, and reaches the maximum value at around 8 GHz. Subsequently, it decreases sharply in the range of 8~16 GHz. Therefore, it can be determined that the three EDCF samples contain the same pore volume (fraction of carbon skeleton), so it can be assumed that the number of hetero-atoms is approximately identical, suggesting that the contribution of conduction loss and defect-induced dipole polarization to EMW attenuation can be cancelled out for them [70]. Furthermore, the difference in EMW absorption performances for these contrast samples can be attributed to the interfacial polarization originated from the surface adsorbed functional group.

Figure 4q, r depicts the 2D projection drawing of EDCF-5 and EDCF-6 in the frequency range of 2~18 GHz at various thicknesses. With the increase of thickness, the appearing frequency of the RL_{\min} shifts towards lower frequency. Compared with EDCF-6, EDCF-3 (Fig. 3j), and EDCF-5 obtain a wider frequency range with the value below -10 dB by adjusting the thickness. As presented in Fig. 4s, the corresponding RL_{\min} value of the three samples at the optimal thickness of them is summarized. Obviously, EDCF-3 also possesses the best RL_{\min} values. Meanwhile, the matching

thickness of EDCF-5 and EDCF-6 is thinner than that of EDCF-3, whereas the widest EAB of EDCF-5 and EDCF-6 appears at the thickness of 1.58 and 1.81 mm respectively, with the corresponding value of 4 GHz (14~18 GHz) and 4.88 GHz (10~15.68 GHz), which is narrower than that of EDCF-3. As displayed in Fig. S12, EDCF-5 obtains the RL_{\min} value of -56.13 dB appearing in X-band at the thickness of 2.39 mm, and the RL_{\min} of EDCF-6 is -30.90 dB at 1.36 mm thickness achieving Ku-band. Apparently, the located frequency of RL_{\min} can be effectively adjusted by changing the pore diameter of different EDCF samples, and it shifts towards high frequency with the increase of pore diameter. Meanwhile, the RL_{\min} value and corresponding matching thickness gradually decreases with the decrease of specific surface area (increase of pore diameter) when the pore volume of the EDCF samples is fixed. Figure S13a, b illustrates the impedance matching and attenuation constant curves of the EDCF-5 and EDCF-6 samples. It can be found that the Z_{in} value of them is closer to 1 just in the high-frequency range, which is consistent with the located frequency of RL_{\min} , manifesting their good impedance matching. Moreover, it should be noted that the variation of specific surface area nearly had no effect on the impedance matching when the pore volume was optimized. As shown in Fig. S13c, d, EDCF-3 obtains the highest α value in the best impedance matching region. Therefore, it also achieves the best EMW absorption performances.

3.2 Equivalent Specific Surface Area Substitution and EMW Absorption Properties of EDCF

In order to investigate the influence of specific surface area on the EMW absorption performances of EDCF samples, two contrast samples, EDCF-7 and EDCF-8 with the same specific surface area and different pore volumes as EDCF-3 were tactfully constructed by introducing silica microspheres with the diameters of 500 nm and 1 μm respectively (as demonstrated in Fig. 4a). The addition content of silica microspheres with the diameter of 500 nm is 1.875 g, while the dosage of silica microspheres with the diameter of 1 μm employed to produce EDCF-8 is approximately 3.75 g. It is believed that EDCF-3, EDCF-7, and EDCF-8 acquire the approximately equivalent adsorbed functional groups, and further stimulate the same surface polarization. In addition, what is different about the EDCF samples

with the same specific surface area is their pore volume ($V_{\text{EDCF-3}} < V_{\text{EDCF-7}} < V_{\text{EDCF-8}}$, $S_{\text{EDCF-3}} = S_{\text{EDCF-7}} = S_{\text{EDCF-8}}$), implying that the content of hetero-atoms decreases from EDCF-3 to EDCF-7 and EDCF-8. Therefore, the difference in EMW absorption performances for these samples can be mainly attributed to the volume proportion of carbon skeleton-related defect-induced dipole polarization. Figure S14 exhibits the SEM images of DC@SiO₂ samples with the same specific surface area, whereas Fig. 5a, b is SEM images of EDCF-7. In this case, it can be observed that numerous pores with the diameter of 500 nm have been created after removing embedded silica microspheres. Moreover, Fig. 5c, d exhibits the SEM images of EDCF-8 with the pore diameter of 1 μm distributed uniformly. Noteworthily, compared with EDCF-5 and EDCF-6 with the same pore diameter, the constructed carbon skeleton of EDCF-7 and EDCF-8 also decreased to a great extent.

Figure S15 displays the XRD pattern and Raman spectra captured from the EDCF samples with the same specific surface area, respectively. Obviously, all of the three EDCF samples feature the same phase and microstructure, indicating that the composition was not affected by the volume or diameter of pores. Besides, their FT-IR spectra were shown in Fig. S16, in which the intensity and integral area of absorption peaks are hardly changed, implying their same type and content of surface-absorbed functional groups. Figure 5e–g are XPS spectra of C, N, and O elements captured from EDCF-3, EDCF-7, and EDCF-8 samples. In Fig. 5e, it can be observed that the integral area of C–C/C–O band and C=O/C=N bond slightly decreases with the increase of pore volume. Meanwhile, as displayed in Fig. 5f, although the relative intensity of the N-containing peak decreases gradually, the integral area ratio of pyridine nitrogen, pyrrole nitrogen and graphite nitrogen of various EDCF samples does not change dramatically, implying that the content of nitrogen atoms is decreasing by the same proportion aroused by the volume increase of pores. Furthermore, Fig. 5g exhibits the O 1s spectra of EDCF samples, and it can be found that the relative intensity of the O1 peak keeps constant, while the O2 peak decreases with the increase of pore volume.

Figure 5h, i display the ϵ' and ϵ'' curves of the EDCF samples with the same specific surface area. The ϵ' curves of the three samples show a decreasing trend versus frequency, and the ϵ'' curves of the three samples show a completely opposite trend in the range of low frequency (2~6 GHz), high frequency (12~18 GHz) and middle frequency (6~12 GHz).

With the other samples, there are multiple resonance phenomena in the curve, indicating the multiple polarization relaxation process occurs [71]. With the same specific surface area, the three samples obtain the same surface defects and adsorption functional groups, that is, the produced interface polarization effect is roughly equivalent. In other words, the higher permittivity values of EDCF-7 than EDCF-8 and EDCF-3 can result from its stronger defect-induced dipole polarization. Besides, the curve of dielectric loss tangent values with frequency variation for EDCF-7 and EDCF-8 was shown in Fig. S17a. Compared with EDCF-3, the curves can be divided into three sections. In the frequency range of 2~6 GHz, the $\tan\delta_\epsilon$ curve of EDCF-7 obtains larger values than EDCF-3 and EDCF-8; in the frequency range of 6~12 GHz, EDCF-7 displays the smallest values, while the change of EDCF-3 and EDCF-8 is almost synchronous in the frequency range of 12~18 GHz. All of them decrease sharply, and EDCF-3 still has the largest values. Furthermore, in Fig. 5j, k, the Cole–Cole curves of EDCF-7 and EDCF-8 appear respectively, and it can be found that EDCF-7 has more Debye relaxation processes than EDCF-3 and EDCF-8, which may acquire stronger polarization loss. The big slope of the linear tail suggests the high conductivity of EDCF-7. According to free electron theory, the conductivity from various samples was shown in Fig. S17b, and EDCF-7 also achieves the highest conductivity value. The conduction loss and polarization loss were calculated respectively, and the corresponding results were shown in Fig. 5l, m. Clearly, the order concerning conduction loss of EDCF samples is the same as that of conductivity, and the polarization loss value versus frequency is similar to ϵ'' curves. In the frequency range of 2~6 GHz and 12~18 GHz, EDCF-7 possesses the highest values, while it obtains the smallest values in the frequency range of 6~12 GHz.

Figure S18 shows the contour chart of EDCF-7 and EDCF-8 samples in the frequency of 2~18 GHz at different thickness. Obviously, the located frequency of the RL_{\min} shows a migrating trend towards lower frequency with the increase of corresponding matching thickness. For sample EDCF-7, the EAB can be adjusted just in the frequency range of 8~18 GHz at different thickness. Meanwhile, EDCF-8 is characterized by the broader adjustable frequency range crossing almost 2~18 GHz and achieves better EAB. Figure 5n exhibits the comparison concerning the RL_{\min} of the EDCF samples with the same specific surface area at respective optimized thickness. Compared with EDCF-3,

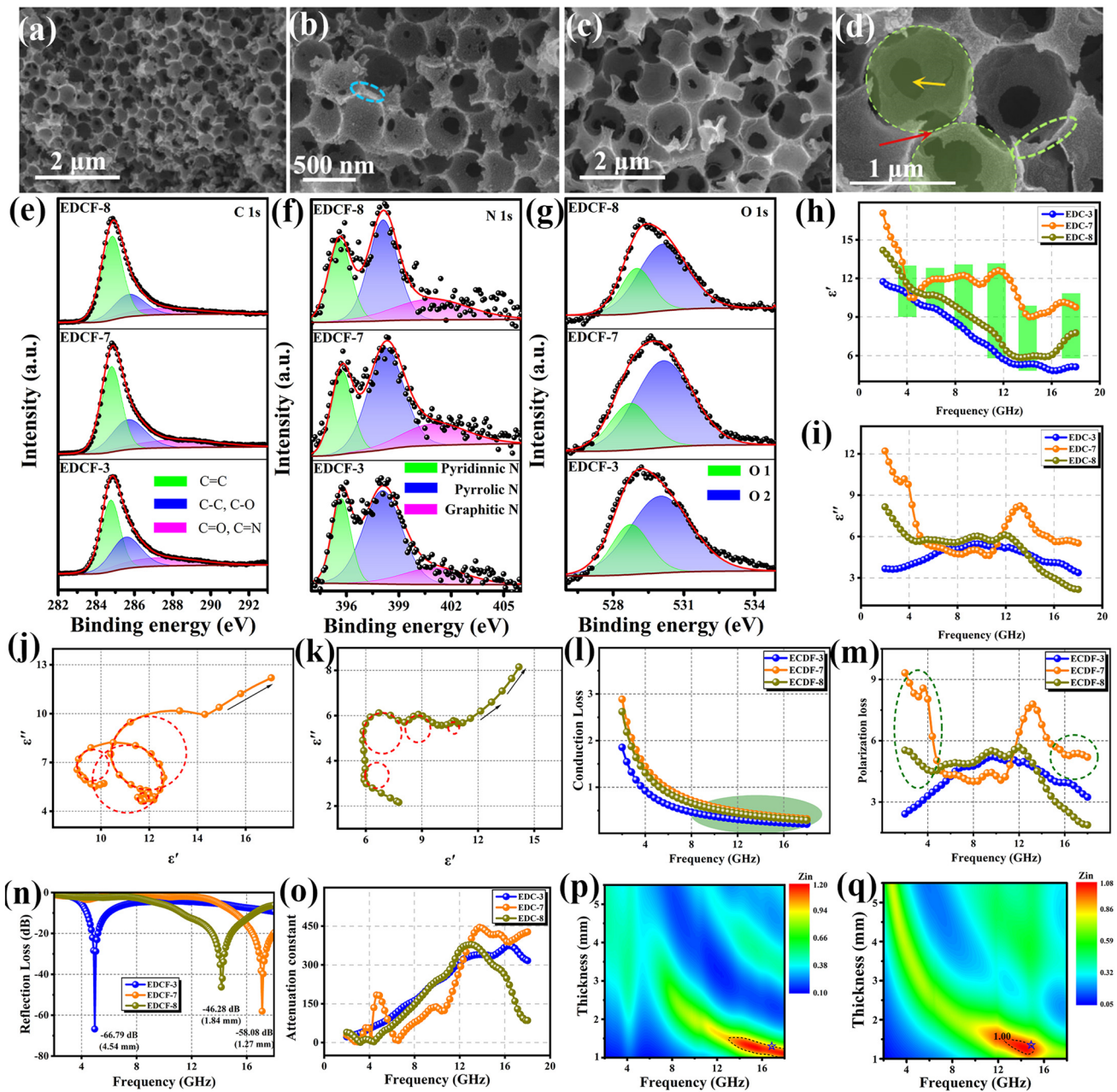


Fig. 5 **a, b** SEM images of EDCF-7 sample; **c, d** SEM images of EDCF-8 sample; high-resolution XPS spectra of **e** C 1s, **f** N 1s, and **g** O 1s of EDCF-3, EDCF-7 and EDCF-8 samples; **h** the real part and **i** the imaginary part of the complex permittivity; **j** Cole–Cole curves of EDCF-7 and **k** EDCF-8; **l** conduction loss and **m** polarization loss of EDCF samples; **n** comparison of the minimum RL curves for EDCF samples with the same specific surface area; **o** attenuation constant and impedance matching of **p** EDCF-7 and **q** EDCF-8

the RL_{min} of EDCF-7 and EDCF-8 appears in Ku band, which is weaker with the values of -58.08 and -46.28 dB respectively whereas the corresponding matching thickness is obviously thinner than the former. Apart from that, Fig. S20a, b displays the impedance matching of EDCF-7

and EDCF-8. Obviously, their proper impedance matching occurs only at thin thickness and high frequency, which is narrower than EDCF-3. Besides, Fig. 5o shows the attenuation constant curves versus frequency, and the EDCF samples with the same specific surface area exhibit similar α

values at different frequency, revealing their EMW attenuation abilities are basically the same, especially in X band and Ku band. At the same time, their nearly equal values suggest that the pore volume has little effect on the α value when the optimal specific surface area is fixed. Furthermore, the contour chart of the impedance matching recorded from EDCF-7 and EDCF-8 was displayed in Fig. 5p, q. It can be found that the value of Z_{in} slightly deviates from 1 with the increase of pore volume, suggesting that the impedance matching is mainly determined by pore volume when the influence of specific surface area is removed first.

3.3 EMW Attenuation Mechanism of EDCF

Figure 6a, b illustrates the RL_{min} and EAB performances of several lightweight carbon absorbers reported recently. Compared with other reported works, the obtained EDCF-7 and EDCF-3 achieve the superior RL_{min} value and EAB performance at thinner thickness, implying that the as-prepared optimal product could be regarded as an attractive candidate for the electromagnetic wave absorber. According to above characterization results, it can be concluded that the polarization loss exhibits an appropriate congruent relationship and synchronous variation tendency with the imaginary part of permittivity, revealing that the dielectric loss is mainly controlled by polarization loss. In addition, there is a very interesting phenomenon that the larger pore volume of EDCF samples with the same specific surface area, the weaker of the RL value. Meanwhile, the larger specific surface area of EDCF samples with the same pore volume, the weaker the RL value. For one thing, the increased specific surface area increases the number of adsorbed functional groups and strengthens the attenuation of incident EMWs caused by interface polarization. For another, the increased pore volume brings more internal defects, acting as the polarization center, that is conducive to dipole polarization and enhances the loss of EMWs. Ideally, the EDCF sample with large specific surface area and pore volume may possess excellent EMW absorption performances. However, it is contradictory to increase or decrease the pore volume and specific surface area at the same time. The EDCF-7 with a compromise-specific surface area and pore volume is regarded as the next-besting sample. In order to evaluate the comprehensive EMW absorption performances, the ratio of RL_{min} to corresponding matching thickness was calculated,

and it should be the more feasible and concerned parameter for the industrial community, as shown in Fig. 6c. Moreover, EDCF-3, EDCF-7 and EDCF-5 take the top three spots of maximum RL values respectively, and at the same time, EDCF-7 with the value of 45.73 dB mm^{-1} acquires much better than other products. Noteworthy, compared with tedious cross experiments, the experimental design strategy employed in this work can quickly determine the optimal sample and offers a more convenient, rapid and accurate optimal scheme for screening the absorption performances.

According to the above analysis, the interfacial polarization mainly originated from the surface defects and absorbed functional groups, which is directly related to the specific surface area, and the effect of dipole polarization on the EMW absorption performances is proportional to the number of defective atoms or heteroatoms in the carbon skeleton (pore volume), indicating that the interfacial polarization and dipole polarization have opposite effects on the electromagnetic parameters of porous carbon-absorbing materials. The EMW absorption performance of the samples is influenced by the interfacial polarization and dipole polarization, which is the result of competition between interface polarization and defect-induced polarization, as shown in Fig. 6d. Besides, the main factors can be summarized as follows: The porous structure increases the interfacial area and corresponding polarization relaxation loss of samples, while the energy is easily dissipated when incident EMWs are irradiated into the porous absorber [72]. Compared with the EDC material without pores, abundant porous structure of EDCF samples can effectively reduce the complex permittivity and promote the impedance matching of the absorber according to Maxwell–Garnett (MG) theory. In this case, it is promised that more EMWs reach the interior of the absorber and expand their effective absorption band. Moreover, the ordered arrangement of pores constructs a conductive network, which not only exerts electrical loss but also is beneficial for the multiple reflection and scattering of electromagnetic waves, enhancing the capacity of converting electromagnetic energy into heat energy [73]. Furthermore, the pyridine-type nitrogen atom that was embedded in the carbon lattice structure can improve the conductivity of EDCF, which is easy to migrate and transmit electrons and dissipates the energy of electromagnetic waves through polarization relaxation. Many defects and functional groups containing N, O, and P atoms result in

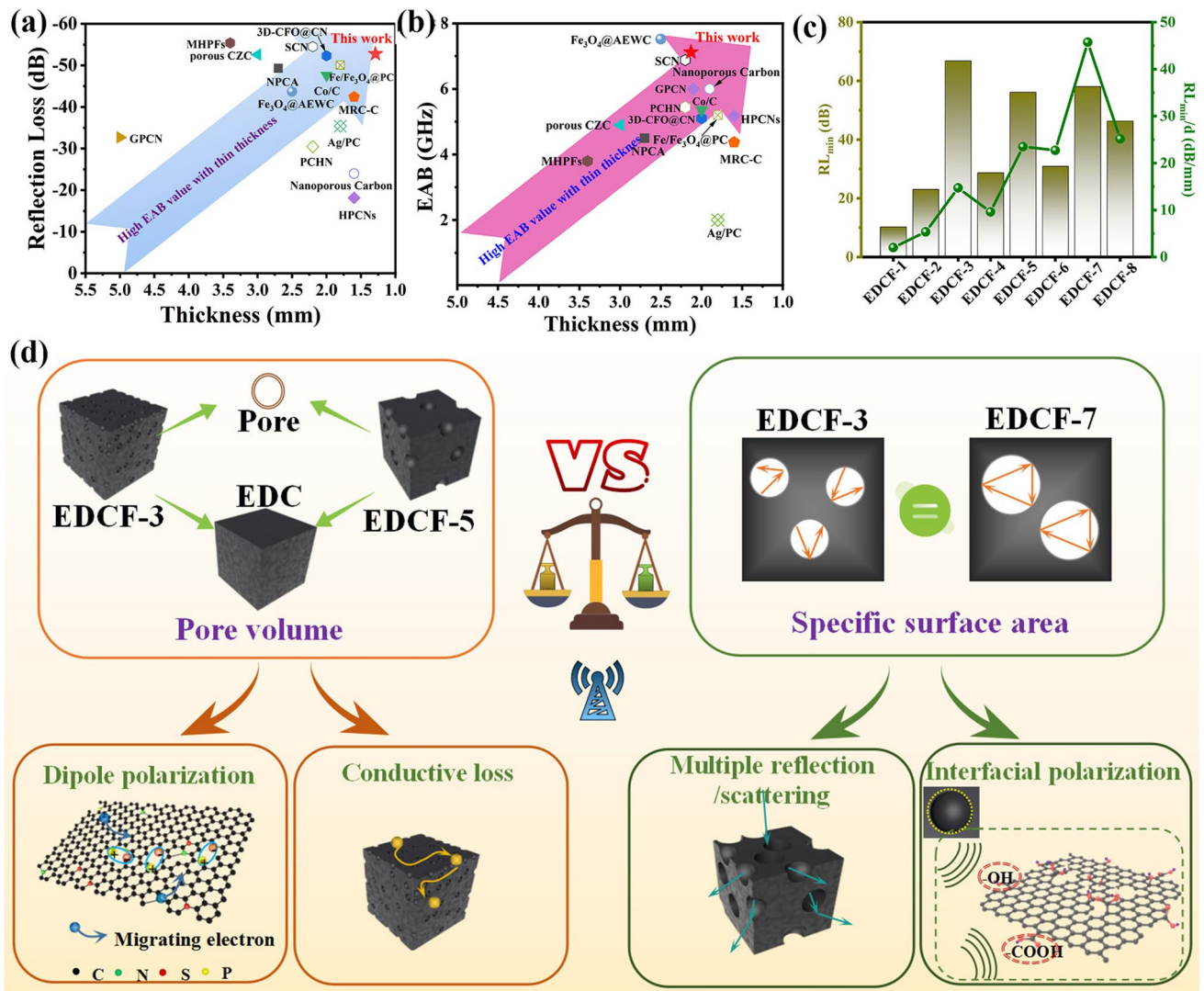


Fig. 6 **a** RL_{min} and **b** EAB versus thickness of carbon-based absorbing materials reported recently; **c** the ratio of RL_{min} to corresponding matching thickness of various EDCF samples; **d** schematic diagram of electromagnetic attenuation strategies for EDCF samples

localized states of Fermi level, which is also conducive to the absorption and attenuation of electromagnetic waves [74]. In the solid-air interface, a large amount of charge in the external electromagnetic field is accumulated, resulting in strong space charge polarization, which plays a positive role in attenuating EMW energy [75]. In other words, the pore volume (carbon skeleton) exerts more influence on the absorption performance than the specific surface area. Appropriate pore volume provides the posterior shield for excellent absorbing performance. In conclusion, the proposed equivalent substitution strategy demonstrates that dipole polarization is the key to determining the dielectric loss behavior of EDCF.

4 Conclusions

According to the principle of equivalent substitution, 3D ordered porous EDCF samples with the same specific surface area and same pore volume were respectively prepared by the template method. The results reveal that the number and diameter of pores not only decrease the density of the absorber but also influence the interfacial polarization and dipole polarization loss of the EMW. The specific surface area can improve the dipole polarization of the product for the purpose of obtaining better EMW absorbing performance. Due to the synergistic effect of interfacial loss and moderate dipole polarization, the optimal sample EDCF-7

obtains excellent RL_{\min} of -58.08 dB at the thickness of 1.27 mm. Meanwhile, EDCF-3 with proper pore structure shows the widest EAB of 7.12 GHz at the thickness of 2.13 mm. More importantly, this work covers the deficiency of the influence of specific surface area on electromagnetic properties, providing a certain reference for the structural design and mechanism research of porous EMW absorbing materials.

Acknowledgements The work reported here was supported by the National Natural Science Foundation of China under Grant No. 52072196, 52002199, 52002200, 52102106, Major Basic Research Program of Natural Science Foundation of Shandong Province under Grant No. ZR2020ZD09, the Natural Science Foundation of Shandong Province under Grant No. ZR2019BEM042, ZR2020QE063, the Innovation and Technology Program of Shandong Province under Grant No. 2020KJA004, and the Taishan Scholars Program of Shandong Province under No. ts201511034. We express our grateful thanks to them for their financial support.

Funding Open access funding provided by Shanghai Jiao Tong University.

Open Access This article is licensed under a Creative Commons Attribution 4.0 International License, which permits use, sharing, adaptation, distribution and reproduction in any medium or format, as long as you give appropriate credit to the original author(s) and the source, provide a link to the Creative Commons licence, and indicate if changes were made. The images or other third party material in this article are included in the article's Creative Commons licence, unless indicated otherwise in a credit line to the material. If material is not included in the article's Creative Commons licence and your intended use is not permitted by statutory regulation or exceeds the permitted use, you will need to obtain permission directly from the copyright holder. To view a copy of this licence, visit <http://creativecommons.org/licenses/by/4.0/>.

Supplementary Information The online version contains supplementary material available at <https://doi.org/10.1007/s40820-022-00900-x>.

References

- X.J. Zeng, X.Y. Cheng, R.H. Yu, G.D. Stucky, Electromagnetic microwave absorption theory and recent achievements in microwave absorbers. *Carbon* **168**, 606–623 (2020). <https://doi.org/10.1016/j.carbon.2020.07.028>
- X.X. Sun, M.L. Yang, S. Yang, S.S. Wang, W.L. Yin et al., Ultrabroad band microwave absorption of carbonized waxberry with hierarchical structure. *Small* **15**(43), 1902974 (2019). <https://doi.org/10.1002/sml.201902974>
- P.B. Liu, S. Gao, G.Z. Zhang, Y. Huang, W.B. You et al., Hollow engineering to Co@N-doped carbon nanocages via synergistic protecting-etching strategy for ultrahigh microwave absorption. *Adv. Funct. Mater.* **31**(27), 2102812 (2021). <https://doi.org/10.1002/adfm.202102812>
- Z.R. Zi, M.Y. Kong, B.W. Yu, Y.Z. Ma, J.Y. Pan et al., Tunable Co/ZnO/C@MWCNTs based on carbon nanotube-coated MOF with excellent microwave absorption properties. *J. Mater. Sci. Technol.* **127**, 153–163 (2022). <https://doi.org/10.1016/j.jmst.2022.04.005>
- Z.H. Wu, Z.Z. Meng, C. Yao, Y. Deng, G.L. Zhang et al., Rice husk derived hierarchical porous carbon with lightweight and efficient microwave absorption. *Mater. Chem. Phys.* **275**, 125246 (2022). <https://doi.org/10.1016/j.matchemphys.2021.125246>
- D.D. Zhi, T. Li, J.Z. Li, H.S. Ren, F.B. Meng, A review of three-dimensional graphene-based aerogels: synthesis, structure and application for microwave absorption. *Compos. Part B Eng.* **211**, 108642 (2021). <https://doi.org/10.1016/j.compositesb.2021.108642>
- L.B. Zhao, Y.Y. Guo, Y.X. Xie, T.T. Cheng, A.L. Meng et al., Construction of SiCNWS@NiCo₂O₄@PANI 1D hierarchical nanocomposites toward high-efficiency microwave absorption. *Appl. Surf. Sci.* **592**, 153324 (2022). <https://doi.org/10.1016/j.apsusc.2022.153324>
- F.Y. Hu, X.H. Wang, S. Bao, L.M. Song, S. Zhang et al., Tailoring electromagnetic responses of delaminated Mo₂TiC₂T_x MXene through the decoration of Ni particles of different morphologies. *Chem. Eng. J.* **440**, 135855 (2022). <https://doi.org/10.1016/j.cej.2022.135855>
- J.B. Cheng, Y.Q. Wang, A.N. Zhang, H.B. Zhao, Y.Z. Wang, Growing MoO₃-doped WO₃ nanoflakes on rGO aerogel sheets towards superior microwave absorption. *Carbon* **183**, 205–215 (2021). <https://doi.org/10.1016/j.carbon.2021.07.019>
- M.T. Qiao, X.F. Lei, Y. Ma, L.D. Tian, X.W. He et al., Application of yolk-shell Fe₃O₄@N-doped carbon nanochains as highly effective microwave-absorption material. *Nano Res.* **11**(3), 1500–1519 (2018). <https://doi.org/10.1007/s12274-017-1767-0>
- Z.J. Li, H. Lin, Y.X. Xie, L.B. Zhao, Y.Y. Guo et al., Monodispersed Co@C nanoparticles anchored on reclaimed carbon black toward high-performance electromagnetic wave absorption. *J. Mater. Sci. Technol.* **124**, 182–192 (2022). <https://doi.org/10.1016/j.jmst.2022.03.004>
- D.W. Xu, S. Yang, P. Chen, Q. Yu, X.H. Xiong et al., Synthesis of magnetic graphene aerogels for microwave absorption by in-situ pyrolysis. *Carbon* **146**, 301–312 (2019). <https://doi.org/10.1016/j.carbon.2019.02.005>
- M. Zhang, H.L. Ling, S.Q. Ding, Y.X. Xie, T.T. Cheng et al., Synthesis of CF@PANI hybrid nanocomposites decorated with Fe₃O₄ nanoparticles towards excellent lightweight microwave absorber. *Carbon* **174**, 248–259 (2021). <https://doi.org/10.1016/j.carbon.2020.12.005>
- H. Du, Q.P. Zhang, B. Zhao, F. Marken, Q.C. Gao et al., Novel hierarchical structure of MoS₂/TiO₂/Ti₃C₂T_x composites for dramatically enhanced electromagnetic absorbing properties. *J. Adv. Ceram.* **10**(5), 1042–1051 (2021). <https://doi.org/10.1007/s40145-021-0487-9>

15. H.T. Guan, Q.Y. Wang, X.F. Wu, J. Pang, Z.Y. Jiang et al., Biomass derived porous carbon (BPC) and their composites as lightweight and efficient microwave absorption materials. *Compos. Part B Eng.* **207**, 108562 (2021). <https://doi.org/10.1016/j.compositesb.2020.108562>
16. W.D. Zhang, X. Zhang, Q. Zhu, Y. Zheng, L.F. Liott et al., High-efficiency and wide-bandwidth microwave absorbers based on MoS₂-coated carbon fiber. *J. Colloid Interface Sci.* **586**, 457–468 (2021). <https://doi.org/10.1016/j.jcis.2020.10.109>
17. H.G. Zhang, Z.R. Jia, A.L. Feng, Z.H. Zhou, C.H. Zhang et al., Enhanced microwave absorption performance of sulfur-doped hollow carbon microspheres with mesoporous shell as a broadband absorber. *Compos. Commun.* **19**, 42–50 (2020). <https://doi.org/10.1016/j.coco.2020.02.010>
18. Z.C. Wang, R.B. Wei, J.W. Gu, H. Liu, C.T. Liu et al., Ultralight, highly compressible and fire-retardant graphene aerogel with self-adjustable electromagnetic wave absorption. *Carbon* **139**, 1126–1135 (2018). <https://doi.org/10.1016/j.carbon.2018.08.014>
19. M. Zhang, H. Lin, S.Q. Ding, T. Wang, Z.J. Li et al., Net-like SiC@C coaxial nanocable towards superior lightweight and broadband microwave absorber. *Compos. Part B Eng.* **179**, 107525 (2019). <https://doi.org/10.1016/j.compositesb.2019.107525>
20. M.L. Cheng, W.L. Ren, H.X. Li, X.G. Liu, S. Bandaru et al., Multiscale collaborative coupling of wood-derived porous carbon modified by three-dimensional conductive magnetic networks for electromagnetic interference shielding. *Compos. Part B Eng.* **224**, 109169 (2021). <https://doi.org/10.1016/j.compositesb.2021.109169>
21. X.M. Huang, X.H. Liu, Z.R. Jia, B.B. Wang, X.M. Wu et al., Synthesis of 3D cerium oxide/porous carbon for enhanced electromagnetic wave absorption performance. *Adv. Compos. Hybrid Mater.* **4**(4), 1398–1412 (2021). <https://doi.org/10.1007/s42114-021-00304-2>
22. H. Zhao, Y. Cheng, W. Liu, L. Yang, B. Zhang et al., Biomass-derived porous carbon-based nanostructures for microwave absorption. *Nano-Micro Lett.* **11**, 24 (2019). <https://doi.org/10.1007/s40820-019-0255-3>
23. R. Shu, G. Zhang, C. Zhang, Y. Wu, J. Zhang, Nitrogen-doping-regulated electromagnetic wave absorption properties of ultralight three-dimensional porous reduced graphene oxide aerogels. *Adv. Electron. Mater.* **7**(2), 2001001 (2020). <https://doi.org/10.1002/aelm.202001001>
24. X.J. Zhu, Y.Y. Dong, Z. Xiang, L. Cai, F. Pan et al., Morphology-controllable synthesis of polyurethane-derived highly cross-linked 3D networks for multifunctional and efficient electromagnetic wave absorption. *Carbon* **182**, 254–264 (2021). <https://doi.org/10.1016/j.carbon.2021.06.028>
25. M.A. Aslam, W. Ding, S. Rehman, A. Hassan, Y. Bian et al., Low cost 3D bio-carbon foams obtained from wheat straw with broadened bandwidth electromagnetic wave absorption performance. *Appl. Surf. Sci.* **543**, 148785 (2021). <https://doi.org/10.1016/j.apsusc.2020.148785>
26. D. Zhao, Q. Zhao, L. Feng, X.Y. Yuan, Y. Liu et al., Honeycomb carbon nanostructure derived from peach gum to yield high microwave absorption. *J. Mater. Sci. Mater. Electron.* **32**(21), 25829–25839 (2020). <https://doi.org/10.1007/s10854-020-04804-7>
27. Z. Xiang, C. Huang, Y.M. Song, B.W. Deng, X. Zhang et al., Rational construction of hierarchical accordion-like Ni@porous carbon nanocomposites derived from metal-organic frameworks with enhanced microwave absorption. *Carbon* **167**, 364–377 (2020). <https://doi.org/10.1016/j.carbon.2020.06.015>
28. P.B. Liu, S. Gao, C. Chen, F.T. Zhou, Z.Y. Meng et al., Vacancies-engineered and heteroatoms-regulated N-doped porous carbon aerogel for ultrahigh microwave absorption. *Carbon* **169**, 276–287 (2020). <https://doi.org/10.1016/j.carbon.2020.07.063>
29. W.B. Deng, T.H. Li, H. Li, X. Liu, A.L. Dang et al., Controllable graphitization degree of carbon foam bulk toward electromagnetic wave attenuation loss behavior. *J. Colloid Interface Sci.* **618**, 129–140 (2022). <https://doi.org/10.1016/j.jcis.2022.03.071>
30. H.L. Lv, Y.H. Guo, Z.H. Yang, T.C. Guo, H.J. Wu et al., Doping strategy to boost the electromagnetic wave attenuation ability of hollow carbon spheres at elevated temperatures. *ACS Sustain. Chem. Eng.* **6**(2), 1539–1544 (2018). <https://doi.org/10.1021/acssuschemeng.7b03857>
31. H.L. Zhu, Y.F. Liu, J. Chen, X. Li, L.H. Gao et al., A one-step ultrasonic spray pyrolysis approach to large-scale synthesis of silica microspheres. *Silicon* **12**(7), 1667–1672 (2020). <https://doi.org/10.1007/s12633-019-00261-y>
32. N. Roosz, M. Euvrard, B. Lakard, L. Viau, A straightforward procedure for the synthesis of silica@polyaniline core-shell nanoparticles. *Colloids Surf. A Physicochem. Eng. Asp.* **573**, 237–245 (2019). <https://doi.org/10.1016/j.colsurfa.2019.04.036>
33. Z.J. Li, H. Lin, S.Q. Ding, H.L. Ling, T. Wang et al., Synthesis and enhanced electromagnetic wave absorption performances of Fe₃O₄@C decorated walnut shell-derived porous carbon. *Carbon* **167**, 148–159 (2020). <https://doi.org/10.1016/j.carbon.2020.05.070>
34. X. Zhang, J. Cheng, Z. Xiang, L. Cai, L. Wang, A hierarchical Co@mesoporous C/macroporous C sheet composite derived from bimetallic MOF and oroxylum indicum for enhanced microwave absorption. *Carbon* **187**, 477–487 (2022). <https://doi.org/10.1016/j.carbon.2021.11.044>
35. X.C. Di, Y. Wang, Z. Lu, R.R. Cheng, L.Q. Yang et al., Heterostructure design of Ni/C/porous carbon nanosheet composite for enhancing the electromagnetic wave absorption. *Carbon* **179**, 566–578 (2021). <https://doi.org/10.1016/j.carbon.2021.04.050>
36. X.A. Li, W.Q. Dong, C. Zhang, W.C. Guo, C.S. Wang et al., Leaf-like Fe/C composite assembled by iron veins interpenetrated into amorphous carbon lamina for high-performance microwave absorption. *Compos. Part A Appl. Sci. Manuf.* **140**, 106202 (2021). <https://doi.org/10.1016/j.compositesa.2020.106202>



37. J.Q. Tao, J.T. Zhou, Z.J. Yao, Z.B. Jiao, B. Wei et al., Multi-shell hollow porous carbon nanoparticles with excellent microwave absorption properties. *Carbon* **172**, 542–555 (2021). <https://doi.org/10.1016/j.carbon.2020.10.062>
38. M.F. Zhou, X.F. Xu, G.P. Wan, P.P. Mou, S.J. Teng et al., Rationally tailoring interface characteristics of ZnO/amorphous carbon/graphene for heat-conduction microwave absorbers. *Nano Res.* (2022). <https://doi.org/10.1007/s12274-022-4521-1>
39. X.J. Zhu, Y.Y. Dong, F. Pan, Z. Xiang, Z.C. Liu et al., Covalent organic framework-derived hollow core-shell Fe/Fe₃O₄@porous carbon composites with corrosion resistance for lightweight and efficient microwave absorption. *Compos. Commun.* **25**, 100731 (2021). <https://doi.org/10.1016/j.coco.2021.100731>
40. M. Rouhani, F.C.N. Hong, Y.R. Jeng, In-situ thermal stability analysis of amorphous carbon films with different sp³ content. *Carbon* **130**, 401–409 (2018). <https://doi.org/10.1016/j.carbon.2018.01.034>
41. D. Geng, S. Zhang, Y.T. Jiang, Z.M. Jiang, M.J. Shi et al., 3D interconnected porous carbon derived from spontaneous merging of the nano-sized ZIF-8 polyhedrons for high-mass-loading supercapacitor electrodes. *J. Mater. Chem. A* **10**(4), 2027–2034 (2022). <https://doi.org/10.1039/D1TA09501C>
42. Y.L. Zhou, N. Wang, X.H. Qu, F.R. Huang, Y.P. Duan et al., Arc-discharge synthesis of nitrogen-doped C embedded TiCN nanocubes with tunable dielectric/magnetic properties for electromagnetic absorbing applications. *Nanoscale* **11**(42), 19994–20005 (2019). <https://doi.org/10.1039/C9NR07111C>
43. V. Dokmai, R. Methaapanon, V. Pavarajarn, Corrosion of amorphous alumina in deionized water under mild condition. *Appl. Surf. Sci.* **499**, 143906 (2020). <https://doi.org/10.1016/j.apsusc.2019.143906>
44. S. Rai, R. Bhujel, J. Biswas, U. Deka, B.P. Swain, Dark and photocurrent response of porous Si/GO-PANI and Si/rGO-PANI heterojunctions for photovoltaics applications. *Mater. Today* **39**, 1848–1851 (2021). <https://doi.org/10.1016/j.matpr.2020.07.373>
45. G. Veber, C.S. Diercks, C. Rogers, W.S. Perkins, J. Ciston et al., Reticular growth of graphene nanoribbon 2D covalent organic frameworks. *Chem* **6**(5), 1125–1133 (2020). <https://doi.org/10.1016/j.chempr.2020.01.022>
46. A. Saral, P. Sudha, S. Muthu, B.R. Rajaraman, S. Selvakumari et al., Quantum mechanical, spectroscopic vibrational analysis, NBO, HOMO-LUMO, and molecular docking studies on 2-Chloroquinoline-3-Carboxamide. *Mater. Today* **50**, 2655–2664 (2022). <https://doi.org/10.1016/j.matpr.2020.07.595>
47. C.Z. Wu, B. Wang, N. Wu, C. Han, X.S. Zhang et al., Molecular-scale understanding on the structure evolution from melamine diborate supramolecule to boron nitride fibers. *Ceram. Int.* **46**(1), 1083–1090 (2020). <https://doi.org/10.1016/j.ceramint.2019.09.075>
48. Q.Q. Li, Y.H. Zhao, X.H. Li, L. Wang, X. Li et al., MOF induces 2D GO to assemble into 3D accordion-like composites for tunable and optimized microwave absorption performance. *Small* **16**(42), 2003905 (2020). <https://doi.org/10.1002/sml.202003905>
49. T.T. Yu, J.F. Qiu, J. Liao, X.Y. Wang, W. Chen et al., Topological transformation strategy for layered double hydroxide@carbon nanofibers as highly efficient electromagnetic wave absorber. *J. Alloys Compd.* **867**, 159046 (2021). <https://doi.org/10.1016/j.jallcom.2021.159046>
50. L.Q. Jin, P.S. Yi, L. Wan, J.S. Hou, P. Chen et al., Thickness-controllable synthesis of MOF-derived Ni@N-doped carbon hexagonal nanoflakes with dielectric-magnetic synergy toward wideband electromagnetic wave absorption. *Chem. Eng. J.* **427**, 130940 (2022). <https://doi.org/10.1016/j.cej.2021.130940>
51. F. Wang, W.H. Gu, J.B. Chen, Y. Wu, M. Zhou et al., The point defect and electronic structure of K doped LaCo_{0.9}Fe_{0.1}O₃ perovskite with enhanced microwave absorbing ability. *Nano Res.* **15**(4), 3720–3728 (2022). <https://doi.org/10.1007/s12274-021-3955-1>
52. F. Wu, Z.H. Liu, J.Q. Wang, T. Shah, P. Liu et al., Template-free self-assembly of MXene and CoNi-bimetal MOF into intertwined one-dimensional heterostructure and its microwave absorbing properties. *Chem. Eng. J.* **422**, 130591 (2022). <https://doi.org/10.1016/j.cej.2021.130591>
53. J.J. Qian, B. Du, M. Cai, C. He, X. Wang et al., Preparation of SiC nanowire/carbon fiber composites with enhanced electromagnetic wave absorption performance. *Adv. Eng. Mater.* **23**(10), 2100434 (2021). <https://doi.org/10.1002/adem.202100434>
54. J.H. Luo, M.N. Feng, Z.Y. Dai, C.Y. Jiang, W. Yao et al., MoS₂ wrapped MOF-derived N-doped carbon nanocomposite with wideband electromagnetic wave absorption. *Nano Res.* (2022). <https://doi.org/10.1007/s12274-022-4411-6>
55. A. Babajanyan, T. Abrahamyan, H. Haroyan, B. Minasyan, T. Yezekyan et al., Microwave response phase control of a graphite microstrip. *Carbon* **193**, 151–156 (2022). <https://doi.org/10.1016/j.carbon.2022.03.020>
56. C.C. Dey, S. Sadhukhan, A. Mitra, M. Dalal, A. Shaw et al., Magnetic energy morphing, capacitive concept for Ni_{0.3}Zn_{0.4}Ca_{0.3}Fe₂O₄ nanoparticles embedded in graphene oxide matrix, and studies of wideband tunable microwave absorption. *ACS Appl. Mater.* **13**(39), 46967–46979 (2021). <https://doi.org/10.1021/acsami.1c10241>
57. M. Zhang, J.H. Zhang, H. Lin, T. Wang, S.Q. Ding et al., Designable synthesis of reduced graphene oxide modified using CoFe₂O₄ nanospheres with tunable enhanced microwave absorption performances between the whole X and Ku bands. *Compos. Part B Eng.* **190**, 107902 (2020). <https://doi.org/10.1016/j.compositesb.2020.107902>
58. Q. Chang, H.S. Liang, B. Shi, X.L. Li, Y.T. Zhang et al., Ethylenediamine-assisted hydrothermal synthesis of NiCo₂O₄ absorber with controlled morphology and excellent absorbing performance. *J. Colloid Interface Sci.* **588**, 336–345 (2021). <https://doi.org/10.1016/j.jcis.2020.12.099>
59. R.Y. Tan, F.K. Zhou, P. Chen, B.S. Zhang, J.T. Zhou, PANI/FeCo@C composite microspheres with broadband microwave

- absorption performance. *Compos. Sci. Technol.* **218**, 109143 (2022). <https://doi.org/10.1016/j.compscitech.2021.109143>
60. J.W. Ge, Y. Cui, J.X. Qian, L. Liu, F.D. Meng et al., Morphology-controlled CoNi/C hybrids with bifunctions of efficient anti-corrosion and microwave absorption. *J. Mater. Sci. Technol.* **102**, 24–35 (2022). <https://doi.org/10.1016/j.jmst.2021.07.003>
61. F. Wu, K. Yang, Q. Li, T. Shah, M. Ahmad et al., Biomass-derived 3D magnetic porous carbon fibers with a helical/chiral structure toward superior microwave absorption. *Carbon* **173**, 918–931 (2021). <https://doi.org/10.1016/j.carbon.2020.11.088>
62. R.D. Guo, D. Su, F. Chen, Y.Z. Cheng, X. Wang et al., Hollow beaded Fe₃C/N-doped carbon fibers toward broadband microwave absorption. *ACS Appl. Mater.* **14**(2), 3084–3094 (2022). <https://doi.org/10.1021/acscami.1c21272>
63. M. Qin, L.M. Zhang, H.J. Wu, Dielectric loss mechanism in electromagnetic wave absorbing materials. *Adv. Sci.* **9**(10), 2105553 (2022). <https://doi.org/10.1002/advs.202105553>
64. M. Qin, L.M. Zhang, X.R. Zhao, H.J. Wu, Lightweight Ni foam-based ultra-broadband electromagnetic wave absorber. *Adv. Funct. Mater.* **31**(30), 2103436 (2021). <https://doi.org/10.1002/adfm.202103436>
65. T.G. Zhu, Y. Sun, Y.J. Wang, H.N. Xing, Y. Zong et al., Controllable synthesis of MOF-derived Fe_xNi_{1-x}@C composites with dielectric-magnetic synergy toward optimized impedance matching and outstanding microwave absorption. *J. Mater. Sci.* **56**(1), 592–606 (2021). <https://doi.org/10.1007/s10853-020-05307-w>
66. J.Q. Tao, J.T. Zhou, Z.J. Yao, Z.B. Jiao, B. Wei et al., Multi-shell hollow porous carbon nanoparticles with excellent microwave absorption properties. *Carbon* **172**, 542–555 (2021). <https://doi.org/10.1016/j.carbon.2020.10.062>
67. C. Zhang, X.A. Li, Y.N. Shi, H.J. Wu, Y.F. Shen et al., Structure engineering of graphene nanocages toward high-performance microwave absorption applications. *Adv. Opt. Mater.* **10**(2), 2101904 (2022). <https://doi.org/10.1002/adom.202101904>
68. X.J. Zhou, J.W. Wen, Z.N. Wang, X.H. Ma, H.J. Wu, Broadband high-performance microwave absorption of the single-layer Ti₃C₂T_x MXene. *J. Mater. Sci. Technol.* **115**, 148–155 (2022). <https://doi.org/10.1016/j.jmst.2021.11.029>
69. M. Zhang, Z.J. Li, T. Wang, S.Q. Ding, G.Y. Song et al., Preparation and electromagnetic wave absorption performance of Fe₃Si/SiC@SiO₂ nanocomposites. *Chem. Eng. J.* **362**, 619–627 (2019). <https://doi.org/10.1016/j.cej.2019.01.039>
70. J.L. Liu, L.M. Zhang, H.J. Wu, Anion-doping-induced vacancy engineering of cobalt sulfoselenide for boosting electromagnetic wave absorption. *Adv. Funct. Mater.* **32**(26), 2200544 (2022). <https://doi.org/10.1002/adfm.202200544>
71. F. Pan, L. Cai, Y.Y. Shi, Y.Y. Dong, X.J. Zhu et al., Phase engineering reinforced multiple loss network in apple tree-like liquid metal/Ni-Ni₃P/N-doped carbon fiber composites for high-performance microwave absorption. *Chem. Eng. J.* **435**, 135009 (2022). <https://doi.org/10.1016/j.cej.2022.135009>
72. C.B. Liang, Z.J. Gu, Y.L. Zhang, Z.L. Ma, H. Qiu et al., Structural design strategies of polymer matrix composites for electromagnetic interference shielding: a review. *Nano-Micro Lett.* **13**, 181 (2021). <https://doi.org/10.1007/s40820-021-00707-2>
73. X.G. Huang, M. Qiao, X.C. Lu, Y.F. Li, Y.B. Ma et al., Evolution of dielectric loss-dominated electromagnetic patterns in magnetic absorbers for enhanced microwave absorption performances. *Nano Res.* **14**(11), 4006–4013 (2021). <https://doi.org/10.1007/s12274-021-3327-x>
74. X.C. Zhang, Y.A. Shi, J. Xu, Q.Y. Ouyang, X. Zhang et al., Identification of the intrinsic dielectric properties of metal single atoms for electromagnetic wave absorption. *Nano-Micro Lett.* **14**, 27 (2022). <https://doi.org/10.1007/s40820-021-00773-6>
75. X. Zhang, L. Cai, Z. Xiang, W. Lu, Hollow CuS microflowers anchored porous carbon composites as lightweight and broadband microwave absorber with flame-retardant and thermal stealth functions. *Carbon* **184**, 514–525 (2021). <https://doi.org/10.1016/j.carbon.2021.08.026>

